



Published in final edited form as:

Nanoscale. 2017 January 05; 9(2): 764–773. doi:10.1039/c6nr07520g.

Development of magneto-plasmonic nanoparticles for multimodal image-guided therapy to the brain

Asahi Tomitaka^a, Hamed Arami^{b,c}, Andrea Raymond^a, Adriana Yndart^a, Ajeet Kaushik^a, Rahul Dev Jayant^a, Yasushi Takemura^d, Yong Cai^e, Michal Toborek^f, and Madhavan Nair^{a,g}

^a Department of Immunology, Herbert Wertheim College of Medicine, Florida International University, Miami, Florida 33199, USA

^b Molecular Imaging Program at Stanford (MIPS), The James H Clark Center, Stanford University, Stanford, California 94305, USA

^c Department of Radiology, Stanford University School of Medicine, Stanford, California 94305, USA

^d Department of Electrical and Computer Engineering, Yokohama National University, Yokohama 240-8501, Japan

^e Department of Chemistry & Biochemistry, Southeast Environmental Research Center, Miami, Florida 33199, Florida International University

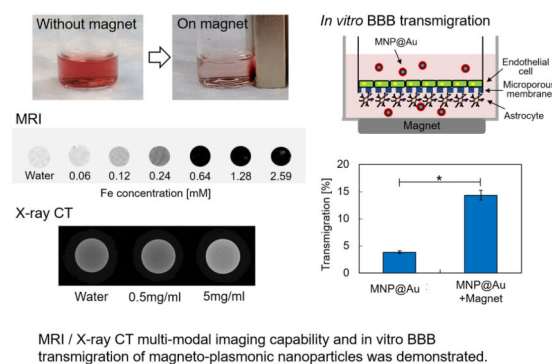
^f Department of Biochemistry and Molecular Biology, University of Miami School of Medicine, Miami, Florida 33136, USA

^g Department of Immunology, Institute of NeuroImmune Pharmacology, Centre for Personalized Nanomedicine, Herbert Wertheim College of Medicine, Florida International University, Miami, Florida 33199, USA

Abstract

Magneto-plasmonic nanoparticles are one of the emerging multi-functional materials in the field of nanomedicine. Their potential for targeting and multi-modal imaging is highly attractive. In this study, magnetic core / gold shell (MNP@Au) magneto-plasmonic nanoparticles were synthesized by citrate reduction of Au ion on magnetic nanoparticle seeds. Hydrodynamic size and optical property of magneto-plasmonic nanoparticles synthesized with the variation of Au ion and reducing agent concentrations were evaluated. The synthesized magneto-plasmonic nanoparticles exhibited superparamagnetic property, and the magnetic property contributed to the concentration-dependent contrast in magnetic resonance imaging (MRI). The imaging contrast from the gold shell part of magneto-plasmonic nanoparticles was also confirmed by X-ray computed tomography (CT). The transmigration study of magneto-plasmonic nanoparticles using an *in vitro* blood–brain barrier (BBB) model proved enhanced transmigration efficiency without disrupting integrity of the BBB, and showed potential to be used for brain diseases and neurological disorders.

Graphical abstract



Introduction

Nanomedicine, which is based on successful administration of nanomaterials to prevent, diagnose, and treat diseases, has attracted attention for the last few decades. Recent progress in nanotechnology has significantly broadened the applications of nanomaterials in biomedical fields. Although nanomedicine has shown promising results in some applications, such as drug delivery and imaging, applications for brain diseases have been limited due to existence of the blood–brain barrier (BBB). The BBB is a diffusion barrier which separates the circulating blood and the brain.^{1–4} Tight junctions between the cerebral endothelial cells limit the transportation of large molecules, and also diffusion of small molecules across the plasma membrane is regulated based on the lipophilicity.⁵ Due to this limited transfer through the BBB, the progress of nanomedicine for brain diseases has not been as fast as progress in other areas. Considerable effort has been directed toward understanding the mechanism of nanoparticle transmigration across the BBB and to improving the targeting efficiency of nanoparticles to the brain non-invasively.² It has been reported that the surface functionalization of nanoparticles with specific ligands can enhance receptor-mediated transcytosis.⁶ The endothelial cells on the BBB express receptors such as transferrin receptors and insulin receptors, which allow ligand functionalized nanoparticles to transmigrate via binding between the ligands on nanoparticles and the receptors on endothelial cells.

Among various nanoparticles developed for nanomedicine, magnetic nanoparticles and Au nanoparticles possess promising properties for theranostics (combination of diagnosis and therapy). Magnetic nanoparticles react with an external magnetic field and show unique properties based on the condition of the magnetic field. A magnetic field gradient exerts magnetic force on magnetic nanoparticles, depending on physical parameters such as particle volume, susceptibility of particles, and a field gradient.⁷ This magnetic force improves the delivery of therapeutic agents to a specific location. When an alternating magnetic field is applied, magnetic nanoparticles induce heat based on hysteresis loss and relaxation losses.⁸ The temperature rise from magnetic nanoparticles can be controlled by changing the strength and frequency of an alternating magnetic field. Due to these unique properties, magnetic nanoparticles have been applied for various biomedical applications, including magnetic resonance imaging (MRI),^{9,10} drug delivery,^{11,12} gene transfection,^{13,14} and hyperthermia (heat treatment).^{15,16} Iron oxide nanoparticles (Fe_3O_4 and $\gamma\text{-Fe}_2\text{O}_3$) are

the most commonly used magnetic nanoparticles for biomedical applications due to their biocompatibility. Coating the iron oxide nanoparticles with various materials such as dextran,¹⁷ polymers,¹⁸ and silica¹⁹ helps functionalize the surface of the nanoparticles and avoids aggregation. These surface-modified and functionalized magnetic nanoparticles have shown great potential as nanocarriers for drug delivery to the brain and imaging probes for brain diseases.^{9,20} In addition, our group has reported enhanced transmigration of magnetic nanoparticles and magneto-electric nanoparticles using magnetic targeting.^{12,21,22}

Gold has been used for numerous medical applications because of its biocompatibility, *in vivo* stability, and versatility in surface functionalization. In addition to these properties, Au nanoparticles possess unique optical property which changes color with their size and shape due to surface plasmon resonance (SPR). When the wavelength of light is much larger than the nanoparticle size and comes to resonance frequency, it causes polarization of the free-electrons in the metal to one surface and oscillates in resonance with the light's frequency.²³ The resonance frequency depends on particle size, shape, dielectric properties, aggregate morphology, surface modification, and surrounding medium.²⁴ The shift of resonance frequency caused by those factors makes gold nanoparticles strong candidates for biosensors.²⁵ This unique optical property makes gold nanoparticles particularly valuable for imaging, including photoacoustic imaging.²⁶ Gold nanoparticles also possess great X-ray attenuation, which makes them attractive contrast agent for X-ray computed tomography (CT).²⁷ The strong absorption of light due to SPR is also converted into heat, which makes gold nanoparticles great heat sources for hyperthermia.²⁸ The combination of magnetic material and gold within the nanoscale system gives multi-functionalities which enable theranostics, multi-modal imaging, and multi-modal image-guided therapies. These are emerging strategies in nanomedicine which allow more efficient treatment with precise targeting and tracking of treatment progress. Several synthesis methods have been reported for magnetic core / gold shell nanoparticles (MNP@Au) such as the microemulsion method,²⁹ iterative hydroxylamine seeding process,³⁰ and seeded growth using citrate reduction.³¹ Although the synthesis of magnetic nanoparticles and gold nanoparticles has been extensively studied, the synthesis of MNP@Au magneto-plasmonic nanoparticles and their physical, magnetic, and optical properties have not been fully investigated for image-guided therapy, especially for applications in the brain. Here, we synthesized MNP@Au magneto-plasmonic nanoparticles by seeding approach using iron oxide nanoparticles as seeds and reducing Au³⁺ using sodium citrate as a reducing agent. The hydrodynamic size and optical properties of MNP@Au synthesized with the variation of HAuCl₄ and sodium citrate concentration were measured, and we evaluated optimal synthesis condition for theranostic applications. The optimized MNP@Au was characterized further for its cytotoxicity and imaging properties. This study is the first report to show the transmigration efficiency of magneto-plasmonic nanoparticles using an *in vitro* BBB model.

Experimental

Materials

Iron(III) chloride (reagent grade, 97%), hydrochloric acid (36.5-38.0%, BioReagent, for molecular biology), sodium sulfite (BioUltra, anhydrous, 98% (RT)), ammonium

hydroxide (28% NH₃ in H₂O, 99.99% trace metals basis), sodium citrate dihydrate (99%, FG), Gold(III) chloride trihydrate (ACS reagent, 49.0% Au basis), potassium thiocyanate (ACS reagent, 99.0%), XTT sodium salt (BioReagent), phenazine methosulfate, Fibronectin from bovine plasma, and Fluorescein isothiocyanate-dextran (molecular weight 40,000 Da) were purchased from Sigma-Aldrich. Ultra Pure Agarose was purchased from Invitrogen. mPEG-Thiol, Mw 5000 was purchased from Laysan Bio, Inc. Human brain astrocytes (HAs), human brain endothelial cells (HBMECs), their culture medium, and poly-L-lysine were purchased from ScienCell Research Laboratories.

Synthesis of magnetic nanoparticles

Magnetic nanoparticles (MNPs) were synthesized by coprecipitation method reported previously.^{21,22} Briefly, 0.487 g of iron(III) chloride was dissolved in 3 ml of 2M hydrochloric acid. 10.33 ml of DI water was added to iron(III) chloride solution, and 0.126g of sodium sulfite dissolved in water was added dropwise under stirring. After the color of the reaction solution changed from yellow to red–light yellow, 80 ml of 0.85M ammonium hydroxide was added dropwise under stirring. The resultant black precipitate was washed with DI water twice using a centrifuge, and neutralized using PBS buffer. After washing, the nanoparticles were heated at 100° C for 1 h.

Citrate coating of magnetic nanoparticles

Hydrochloric acid (2M) was added to 10 ml of 2 mg/ml MNPs, and sonicated for 0.5h. 10 ml of 20 mg/ml sodium citrate was added to the MNPs solution, and sonicated for another 20 min using bath sonication, followed by 5 min probe sonication using a Sonic Dismembrator 150E (Fisher Scientific) at 30% amplitude. Citrate-coated MNPs were purified with distilled water using a centrifuge. Then, purified citrate-coated MNPs were sonicated using a probe sonicator at 20% amplitude, and aggregated nanoparticles were removed by centrifugation at 10,000g for 10 min.

Synthesis of MNP@Au magneto-plasmonic nanoparticles

Citrate-coated MNPs (MNP-citrate, 0.05 mM) dispersed in additional sodium citrate solution were sonicated for 5 min using a probe sonicator at 20% amplitude prior to gold coating. 20 ml of MNP-citrate in sodium citrate solution was heated to boiling temperature with stirring at 300 rpm. Then HAuCl₄ was added to the MNP-citrate and stirred for 4 min. The resulting magnetic core / gold shell nanoparticles (MNP@Au) were collected using a magnet and redispersed into distilled water. The reaction was carried out with the initial HAuCl₄ varied from 1.5 to 15 μmol and fixed concentrations of sodium citrate (5 mM) to evaluate HAuCl₄ dependence on synthesis. For the reactions with variable concentrations of sodium citrate, the initial amount of HAuCl₄ was fixed at 15 μmol and the concentrations of sodium citrate were varied from 0.5 mM to 20 mM.

Characterization of MNP@Au magneto-plasmonic nanoparticles

The iron and gold concentrations were determined using an inductively coupled plasma mass spectrometer (ICP-MS, Perkin Elmer Sciex, model ELAN DRC-II). Samples were dissolved in aqua regia and diluted by deionized water prior to the measurement. Optical

properties of MNP@Au were determined by measuring absorbance using a UV-Visible Spectrophotometer (HITACHI U-2910). Samples were diluted with distilled water to the Fe concentration of 10 µg/ml. The hydrodynamic sizes and zeta potentials of MNP@Au were measured by Zetasizer Nano-ZS (Malvern instruments). 10 µl of MNP@Au were dispersed in 1 ml distilled water. Transmission electron microscopy (TEM) images were acquired using a Phillips CM-200 200 kV transmission electron microscope operated at 80 kV. X-ray powder diffraction (XRD) pattern of MNP@Au was recorded with a Siemens D-5000 diffractometer with Cu K α radiation ($\lambda = 0.154056$ nm). The magnetization curves of MNP-citrate and MNP@Au were measured using a vibrating sample magnetometer (VSM-3, Toei Kogyo) equipped with an electromagnet (TEM-WFR7, Toei Kogyo) and a gaussmeter (Model 421, Lake Shore Cryotronics, Inc.). The measurement was conducted at room temperature with a maximum field of 780 kA/m.

Multimodal imaging property of MNP@Au magneto-plasmonic nanoparticles

The MRI property of MNP@Au was evaluated in a 30cm horizontal bore 7-Tesla MRI system (Bruker Biospin). An aqueous solution of nanoparticles (100 µl) was placed into a polymerization chain reaction (PCR) tube and fixed with 1wt% agar. Sample temperature was maintained at room temperature. The transverse relaxation time (T_2)-weighted images were obtained with the following parameters: pulse repetition time (TR) 2000 ms, echo time (TE) 5.21ms, slice thickness (ST) 1mm, and number of acquisitions (NA) 12. Micro-CT imaging was conducted using Skyscan1172 (Bruker) with a source voltage of 40 kV and a current of 250 µA. CT values were estimated in Hounsfield units (HU) by calibration with water and air as 0 HU and -1000 HU, respectively.

PEGylation of MNP@Au magneto-plasmonic nanoparticles

Polyethylene glycol (PEG) has been used to improve the stability of nanoparticles and increase circulation time for *in vivo* applications. The optimized MNP@Au was coated with PEG to improve stability in biological buffer to allow for further cytotoxicity and *in vitro* BBB experiments. For the coating process, mPEG-Thiol (100 ml of 0.5 mg/ml) was added to 15 mg of MNP@Au and stirred at 300 rpm overnight. PEG-coated MNP@Au (MNP@Au-PEG) was purified three times using a centrifuge and sonicated for 1 min at 20% amplitude using a probe sonicator.

Cytotoxicity of MNP@Au and MNP@Au-PEG

The cytotoxicity of MNP@Au and MNP@Au-PEG was evaluated by XTT (Sodium 3,3'-[(Phenylamino)carbonyl]-3,4-tetrazolium)-bis(4-methoxy-6-nitro)benzene sulfonic acid hydrate) assay. Primary human astrocytes were seeded in a 96-well cell culture plate at a density of 1×10^4 cells/well. After 24h of incubation at 37° C, the medium was replaced with 100 µl of fresh medium containing 10–100 µg/ml of MNP@Au. After 24 and 48 hr incubation, cells were washed twice with PBS and 100 µl of fresh medium was added. The XTT/PMS mixture solution was prepared by mixing XTT and phenazine methosulfate (PMS) immediately before use. 25 µl of XTT/PMS mixture solution was added to each well and incubated at 37 µC for 4 hr. Absorbance was measured at 450 nm using a microplate reader (Synergy HT, multi-mode microplate reader, BioTek).

Experiments were performed in quadruplicate replicates (N=3). The results are represented as the mean \pm standard deviation. Statistical analysis was performed using one-way analysis of variance (ANOVA) followed by Tukey's multiple comparison test and difference was considered significant at $P < 0.05$.

***In vitro* blood-brain barrier (BBB) model**

The BBB model was established as described earlier.^{21,22} In brief, the *in vitro* BBB model was developed in a bicompartamental transwell culture plate (Corning Life Sciences). The upper chamber of this plate was separated from the lower chamber by a 10 μm thick polycarbonate membrane with 3.0 μm pores. In a 24-well cell culture plate with pore density of 2×10^6 pores/ cm^2 and cell growth area of 0.33 cm^2 , 2×10^5 primary human brain microvascular endothelial cells (HBMECs) and human astrocytes (HAs) were grown to confluence on the upper side and the underside of the inserts, respectively. The further experiment was conducted within 6 days after seeding the cells, and establishment of the BBB integrity was confirmed by the transendothelial electrical resistance (TEER) measurement.

The transmigration study was conducted by adding 5 μg of MNP@Au-PEG magneto-plasmonic nanoparticles to the upper chamber and incubating at 37°C for 24h with or without magnet (magnetic field of 150 mT at the surface of culture plate) below the cell culture plate. After incubation, the media containing the nanoparticles was collected from both the upper and lower chambers and centrifuged to precipitate nanoparticles. The concentration of the nanoparticles re-dispersed in water was measured using a UV-Visible Spectrophotometer. Transmigration efficiency was calculated as

$$\text{Transmigration efficiency } [\%] = \frac{(\text{nanoparticle concentration in lower chamber})}{((\text{nanoparticle concentration in lower chamber}) + (\text{nanoparticle concentration in upper chamber}))} \times 100$$

The effect of nanoparticle exposure on the integrity of the *in vitro* BBB was determined by measuring TEER using Millicell ERS microelectrodes (Millipore) after exposure of the nanoparticles to the BBB model.

The effect of nanoparticle exposure to the permeability of the *in vitro* BBB model was determined by measuring the transfer of FITC-dextran through the BBB model. Briefly, 100 μg of FITC-dextran was added to the upper chamber and further incubated for 4h. Samples were collected from the lower chamber and fluorescence was measured at an excitation wavelength of 485 nm and an emission wavelength of 520 nm using a microplate reader (Synergy HT, multi-mode microplate reader, BioTek). The permeability was calculated as a percentage of FITC-dextran transported across the BBB model compared to FITC-dextran transported across the inserts without cells. Experiments were performed in duplicate replicates (N=3). The results are represented as the mean \pm standard deviation.

Results and discussion

Synthesis of MNP@Au magneto-plasmonic nanoparticles

MNP@Au magneto-plasmonic nanoparticles were synthesized by seeding approach with modification.^{32,33} Brown *et al* synthesized large colloidal Au nanoparticles by growing small Au nanoparticles (seeds) with adding HAuCl₄ and citrate at boiling temperature.³² The surface-catalyzed reduction, which is reduction of Au³⁺ on the surface of seeds without new particle nucleation, allowed production of large Au nanoparticles with uniform size and shape.³³ By modifying this method, core-shell nanoparticles of magnetic nanoparticles core and Au shell have been synthesized by reducing Au³⁺ on magnetic nanoparticle seeds.^{31,34} Since narrow size distribution of seeds is the key for monodispersity of MNP@Au, we conducted surface modification of MNPs with sodium citrate and removed aggregation using a centrifuge prior to Au coating. The average hydrodynamic size of citrate-coated MNPs (MNP-citrate) was 63 ± 14 nm. After citrate coating, additional sodium citrate was added to the MNP-citrate as a reducing agent and heated to boiling temperature, followed by the addition of Au ions. The clear brown color of MNPs became dark brown after addition of Au ions and gradually turned into red.

Characterization of MNP@Au magneto-plasmonic nanoparticles

Figure 1(a-c) shows the Au to Fe weight ratio, absorbance, and hydrodynamic sizes of MNP-citrate and MNP@Au synthesized with initial HAuCl₄ varied from 1.5 to 15 μmol and fixed concentration of sodium citrate (5 mM). The color of MNP@Au changed from brown to red by increasing the amount of HAuCl₄ based on the absorbance of the particles. An increase of absorbance at the wavelength below 460 nm was observed for MNP-citrate, which corresponded with previous reports.³¹ It has been reported that iron oxides show absorption at the wavelength of 250–400 nm due to ligand to metal charge transition.³⁵ The optical property of MNP@Au largely depends on the particle size, shape, and thickness of the Au shell due to surface plasmon resonance (SPR), which is based on the oscillation of free-electrons polarized to one surface under light with oscillation frequency.²³ There were no apparent absorbance peaks for MNP-citrate and MNP@Au synthesized with 1 μmol HAuCl₄ at the wavelength above 460 nm. With increasing the amount of HAuCl₄, significant absorbance appeared at the wavelength between 460 nm and 600 nm. This can be explained by the increase of Au to Fe ratio proportionally with the amount of initial HAuCl₄. The peak of absorbance was observed at 526 nm for MNP@Au synthesized with 15 μmol HAuCl₄. Average hydrodynamic sizes of MNP@Au synthesized with 1.5, 3, 7.5, and 15 μmol HAuCl₄ were 84, 63, 61, and 57 nm, respectively.

Table 1 shows synthesis conditions and characterizations of MNP@Au synthesized with initial HAuCl₄ of 15 μmol and sodium citrate concentration varied from 0.5 to 20 mM. Figure 1(d-f) illustrates the Au to Fe weight ratio, absorbance, and Au to Fe weight ratio of MNP@Au decreased significantly with increasing the concentration of sodium citrate from 0.5 mM to 2 mM and increased with further increases of sodium citrate. This indicates that the particle size of MNP@Au varies with the concentration of sodium citrate during synthesis. In Figure 1(c), MNP@Au synthesized with 0.5 mM sodium citrate showed SPR peak at the wavelength of 556 nm, and the absorbance at the SPR peak was the highest

among other MNP@Au. Those synthesized with 1 mM and 20 mM sodium citrate showed broader SPR spectra, and similar broad SPR spectrum with lower absorbance was observed for those synthesized with 2 mM sodium citrate. MNP@Au synthesized with 5 mM sodium citrate showed a narrower SPR spectrum at the wavelength of 526 nm. The citrate reduction method is the most commonly used method for gold nanoparticle synthesis. It has been reported that the nanoparticle size was reduced with increasing sodium citrate concentration,³⁶ and further increases of sodium citrate concentration increased the particle size.³⁷ This trend corresponds with the reduced Au to Fe ratio with increasing sodium citrate concentration and increase of Au to Fe ratio with further increase of sodium citrate. This size variation with the concentration of sodium citrate has been determined by the solution pH during reaction which affects to the stability of nanoparticles and reactivity of Au (composition of Au³⁺).^{37,38} The pKa value of citric acid is 3.2, 4.8, and 6.4. Above pH 6.4, the carboxyl groups in sodium citrate are fully deprotonated, and the resulting negative zeta potential keeps the stability of nanoparticles by repulsion. On the other hand, when the pH of reaction solution is low, the carboxyl groups are protonated, lose repulsion between nanoparticles, and consequently cause aggregation of nanoparticles. In reaction solutions with lower pH (pH 3.2 and 5.5 for 0.5 mM and 1 mM sodium citrate, respectively), it is possible that aggregation of nanoparticles occurred in the sodium citrate solution during growth of the Au shell, and the aggregation was reduced with increasing the sodium citrate concentration. The reduction of Au to Fe ratio with increasing sodium citrate concentration up to 2 mM can also be explained by pH dependent redox potential of Au complexes. AuCl₄ is formed when HAuCl₄ is totally dissociated in aqueous solutions. As the solution pH increases, hydroxyl containing gold complexes are formed, and the complex changes from AuCl(OH)⁻ to Au(OH)₂⁻,³⁸ which weakens reactivity. On the other hand, in the reaction solution with pH 7.0 (5 mM to 20 mM sodium citrate), it is possible that the reduction of Au³⁺ was increased by increasing the amount of sodium citrate, which resulted in higher Au to Fe ratio.

In Figure 1(f), the average hydrodynamic sizes of MNP@Au synthesized with 0.5, 5, and 20 mM sodium citrate were 64, 57, and 95 nm, respectively, and MNP@Au synthesized with 1 and 2 mM sodium citrate showed polydispersity. The color of MNP@Au varied between purple and red. It is known that SPR is dependent on particle size, shape, dielectric properties, aggregate morphology, surface modification, and surrounding medium.²⁴ For example, the red shift and broadening of the absorbance have been reported as the hydrodynamic size of gold nanoparticles increases.³⁹ It is possible that the broad SPR peak of MNP@Au synthesized with 1 mM, 2 mM, and 20 mM sodium citrate is caused by their polydispersity or larger hydrodynamic size as compared to MNP@Au synthesized with 0.5 mM and 5 mM sodium citrate. As shown in Figure 1(e) inset, MNP@Au synthesized with 5 mM sodium citrate exhibited the narrowest SPR peak at the wavelength of 526 nm, followed by MNP@Au synthesized with 0.5 mM sodium citrate, which showed highest SPR peak at wavelength of 556 nm. Hydrodynamic size is one of the important factors for nanoparticle-based *in vivo* applications. Nanoparticles smaller than 10 nm are rapidly removed by renal clearance, and larger nanoparticles (>200 nm) are removed by the reticuloendothelial system (RES) of the spleen and liver.⁴⁰ Therefore, the optimal hydrodynamic size of nanoparticle formulation for *in vivo* applications is known to be 10–100 nm.⁴¹ This excludes MNP@Au

synthesized with 1 mM and 2 mM sodium citrate, which showed multiple peaks in their hydrodynamic sizes, and MNP@Au synthesized with 20 mM sodium citrate, which showed hydrodynamic size distribution between 51 nm to 220 nm. Comparing MNP@Au synthesized with 0.5 mM and 5 mM sodium citrate, serious aggregation was observed for MNP@Au synthesized with 0.5 mM sodium citrate within a month after synthesis, while MNP@Au synthesized with 5 mM sodium citrate remained stable. Considering these factors, we conducted further characterization on the MNP@Au synthesized with 15 μmol HAuCl_4 and 5mM sodium citrate.

Figure 2(a) shows the TEM image of the MNP@Au. The average particle diameter of 14.5 nm and spherical morphology were observed from this TEM image. Since the MNP core showed an average diameter of 10 nm and spherical morphology in our previous report,¹² the average thickness of the shell is calculated to be 2.3 nm.

Figure 2 (b) shows the X-ray diffraction (XRD) pattern of MNP@Au. The XRD pattern of MNPs has been reported in our previous report.²¹ The XRD pattern of MNP@Au showed sharp peaks at 38.2°, 44.4°, 64.5° and 77.7°, which can be indexed to the (1 1 1), (2 0 0), (2 2 0) and (3 1 1) planes, respectively. The sharp peak at 38.2° could be the synergistic effect from (3 1 1) plane of MNP core and (1 1 1) plane of Au shell. It has been reported that the diffraction from the core can be observed by the penetration of X-ray through the gold shell layer,⁴² and the diffraction from the gold shell dominates as the thickness of the gold shell increases.⁴³

Figure 2 (c) and (d) show the magnetization curves of MNP-citrate and MNP@Au, and the picture of MNP@Au attracted by a magnet. The MNPs showed superparamagnetic properties before and after Au coating. The saturation magnetization of MNP-citrate and MNP@Au were 27 emu/g and 22 emu/g, which are 36% and 29% of the bulk saturation value for hematite (76 Am^2/kg or emu/g⁴⁴), respectively. Significant decrease in saturation magnetization of MNPs after Au coating due to diamagnetic contribution of the Au shell has been reported previously³¹. However, MNP@Au showed slightly lower saturation magnetization and higher susceptibility compared to MNP-citrate, contrary to the large portion of Au (61%) in MNP@Au. Since magnetic nanoparticles respond to the magnetic field gradient in a size dependent manner, magnetic separation has been used to separate larger particles.⁴⁵ We expect that MNP@Au with small saturation magnetization was removed during purification process using a magnet, and MNP@Au with only large magnetization was collected after purification.

Multimodal imaging property of MNP@Au magneto-plasmonic nanoparticles

MRI and micro-CT scan were conducted to demonstrate multimodal imaging capability of MNP@Au magneto-plasmonic nanoparticles. Figure 3 (a) and (b) show the T_2 -weighted MR images and transverse relaxivity of MNP@Au as a function of Fe concentration. Stronger negative contrast was observed with increasing the concentration of Fe. In addition, linear correlation between transverse relaxivity and Fe concentration was observed. The T_2 relaxivity was calculated to be 60 $\text{mM}^{-1}\cdot\text{s}^{-1}$.

The micro-CT images and CT values of MNP@Au are shown in Figure 3 (c) and (d). The brightness increased in a concentration-dependent manner, and MNP@Au showed CT attenuation values of 24 Hounsfield units (HU) and 178 HU at the concentrations of 0.5 mg/ml and 5 mg/ml, respectively. This result corresponded to previous reports showing the concentration dependence of CT value from Au nanoparticles due to X-ray attenuation of gold.⁴⁶ There is a growing interest in using Au nanoparticles as CT contrast agents because of the higher X-ray attenuation coefficient of gold compared to iodine which is currently used in the clinic.⁴⁷ Since X-ray attenuation is not efficient and the blood circulation time of iodinated CT contrast agents is short,⁴⁸ the nanoparticles containing heavy metal are the great candidates as novel CT contrast agents. These strong contrasts in MRI and X-ray CT from MNP@Au suggest that the magneto-plasmonic nanoparticles have potential as a strong multi-modal imaging probes for MRI and X-ray CT.

Cytotoxicity of MNP@Au and MNP@Au-PEG

Figure 4 shows the impacts of MNP@Au and PEG-coated MNP@Au (MNP@Au-PEG) on cell viability evaluated by XTT assay. The viability of human astrocytes decreased to 74% and 69% after exposure of MNP@Au at the concentration of 100 µg/ml for 24h and 48h, respectively. No significant decrease in the viability was observed for the cells exposed to MNP@Au-PEG at the concentrations lower than 100 µg/ml.

Although magneto-plasmonic nanoparticles have been studied for biosensor applications, they are relatively new in *in vitro* and *in vivo* biomedical applications. Thus, there are fewer studies evaluating the biocompatibility of MNP@Au nanoparticles compared to well-studied iron oxide nanoparticles and gold nanoparticles. Moreover, there is no viability study conducted on primary human astrocyte cells to the best of our knowledge. Some researchers have conducted viability assays on cell lines including L929 fibroblast,⁴⁹ HeLa cells,⁵⁰ H9c2 cardiomyoblasts, and MCF-7 breast carcinoma cells⁵¹ after exposing MNP@Au. Significant viability reduction was not observed in L929 fibroblast and HeLa cells, and 14% and 23% reductions were observed in cultured H9c2 cardiomyoblasts and MCF-7 breast carcinoma cells after 24h exposure of nanoparticles at the concentration of 500 µg/ml. This reduction range is similar to our results on primary human astrocytes. Also, no significant influence on the viability of human mesenchymal stem cells (hMSCs) and U87 glioma cells has been reported after exposing hybrid nanoparticles containing Fe₃O₄ core coated with gold nanoparticles.^{52,53}

Since MNP@Au is less stable in media due to lack of PEG chain, we expect that aggregation of MNP@Au caused the reduction of viability contrary to the PEG-coated MNP@Au which showed no viability reduction.

In vitro blood–brain barrier (BBB) model

The transmigration across the blood–brain barrier (BBB) is very limited due to the presence of tight junctions between capillary endothelial cells.⁵⁴ This limitation restricts application of nanoparticles in the brain. Therefore, it is essential to evaluate the transmigration capability of nanoparticles across the BBB for brain-targeted applications. The transmigration efficiency of magneto-plasmonic nanoparticles was evaluated using the *in*

in vitro BBB model prepared with primary human brain microvascular endothelial cells (HBMECs) and human astrocytes (HAs) (Figure 5 (a)). PEG-coated MNP@Au (MNP@Au-PEG) were used for this experiment due to their high viability and stability in media. The transmigration efficiency of magneto-plasmonic nanoparticles was determined by measuring the concentration of the nanoparticles crossed the *in vitro* BBB model. The transmigration efficiency of the nanoparticles in the absence and in the presence of a magnetic field is shown in Figure 5 (b). Only 3.8% of the nanoparticles were able to cross the BBB without a magnetic field. Compared to this low transmigration efficiency due to the high integrity of the BBB, the presence of a magnetic field increased transmigration efficiency significantly which was four-fold increase compared to the transmigration in the absence of a magnetic field.

The integrity of the BBB model was evaluated by TEER measurement. Figure 5 (c) shows TEER values of the control BBB without nanoparticles or a magnetic field from a magnet, with nanoparticles in the absence of a magnetic field, and with nanoparticles in the presence of a magnetic field from a magnet. Since a TEER value around $200 \Omega/\text{cm}^2$ is considered as the formation of the BBB,⁵⁵ $195.5 \pm 13.0 \Omega/\text{cm}^2$ from the control BBB proves that the BBB model is already formed and intact. The TEER values of the BBB with nanoparticles in the absence and in the presence of a magnetic field were 194.2 ± 5.2 and $197.7 \pm 4.7 \Omega/\text{cm}^2$, respectively. Compared to the control BBB, there was no effect on the integrity of the BBB model after exposure to nanoparticles and magnetic field.

Permeability across the BBB model was then determined by measuring the transfer of FITC-dextran.⁵⁶ Figure 5 (d) shows the percentage of FITC-dextran transfer across the BBB calculated with respect to the FITC-dextran transfer across untreated insert without cells. The FITC-dextran transfer of the control BBB, the BBB with nanoparticles in the absence of a magnetic field, and the BBB with nanoparticles in the presence of a magnetic field was 22%, 22%, and 20%, respectively. This shows that exposing nanoparticles along with an external magnetic field does not induce an effect on the permeability of the BBB model. Overall, the results in Figure 5 indicate that the presence of a magnetic field increases the transmigration of magneto-plasmonic nanoparticles significantly without affecting the integrity and permeability of the BBB.

In this study, we developed MNP@Au magneto-plasmonic nanoparticles optimized for image-guided therapy for brain diseases and demonstrated the biocompatibility and capability of these nanoparticles to cross the BBB. The MRI and X-ray CT contrasts generated by the magneto-plasmonic nanoparticles will enable image-guided therapy for various brain diseases such as brain tumors, Alzheimer's disease, and human immunodeficiency virus (HIV) infection. Furthermore, the magneto-plasmonic nanoparticles can be used for a wide range of biomedical applications including hyperthermia or photothermal therapy, radiation sensitizer, and stem cell tracking.

Conclusions

Magneto-plasmonic nanoparticles with magnetic core / gold shell structure were synthesized by reduction of Au ion on magnetic nanoparticle seeds using sodium citrate. The

hydrodynamic sizes and optical properties of magneto-plasmonic nanoparticles varied with changing Au ion and sodium citrate concentrations. The smallest hydrodynamic size and narrowest SPR peak were observed with the nanoparticles synthesized with 15 μmol HAuCl_4 and 5mM sodium citrate. The synthesized magneto-plasmonic nanoparticles exhibited superparamagnetic property, and T_2 -weighted MRI and X-ray CT imaging contrasts in a concentration-dependent manner. The transmigration of magneto-plasmonic nanoparticles across the *in vitro* blood–brain barrier (BBB) was significantly enhanced without disrupting the integrity of the BBB, when an external magnetic field was applied. These results demonstrate the potential of magnetic-gold core-shell magneto-plasmonic nanoparticles for brain-targeted theranostics and image-guided therapy.

Acknowledgements

We would like to acknowledge Advance Materials Engineering Research institute (AMERI) at FIU for TEM and XRD, Trace Evidence Analysis Facility at FIU for ICP-MS, and Micro Photonics Inc. for Micro-CT scanning. This work was supported by NIH grants 1R01DA037838-01, 1R01DA040537-01, and R01DA034547.

Notes and references

1. Ballabh P, Braun A, Nedergaard M. *Neurobiol. Dis.* 2004; 16:1–13. [PubMed: 15207256]
2. Nair M, Jayant RD, Kaushik A, Sagar V. *Adv. Drug Deliv. Rev.* 2016; 103:202–217. [PubMed: 26944096]
3. Kaushik A, Dev Jayant R, Sagar V, Nair M. *Expert Opin. Drug Deliv.* 2014; 11:1635–1646. [PubMed: 24986772]
4. Jayant RD, Sosa D, Kaushik A, Atluri V, Vashist A, Tomitaka A, Nair M. *Expert Opin. Drug Deliv.* 2016 **in print**.
5. Ohtsuki S, Terasaki T. *Pharm. Res.* 2007; 24:1745–1758. [PubMed: 17619998]
6. Wohlfart S, Gelperina S, Kreuter J. *J. Control. Release.* 2012; 161:264–273. [PubMed: 21872624]
7. Pankhurst QA, Connolly J, Jones SK, Dobson J. *J. Phys. D. Appl. Phys.* 2003; 36:167–181.
8. Rosensweig REE. *J. Magn. Magn. Mater.* 2002; 252:370–374.
9. Abakumov MA, Nukolova NV, Sokolsky-Papkov M, Shein SA, Sandalova TO, Vishwasrao HM, Grinenko NF, Gubsky IL, Abakumov AM, Kabanov AV, Chekhonin VP. *Nanomedicine Nanotechnology, Biol. Med.* 2015; 11:825–833.
10. Tomitaka A, Jo J, Aoki I. *Inflamm. Regen.* 2014; 34:45–55.
11. Chen J, Shi M, Liu P, Ko A, Zhong W, Liao W, Xing MMQ. *Biomaterials.* 2014; 35:1240–1248. [PubMed: 24239110]
12. Jayant RD, Atluri VSR, Agudelo M, Sagar V, Kaushik A, Nair M. *Int. J. Nanomedicine.* 2015; 10:1077–1093. [PubMed: 25709433]
13. Kami D, Kitani T, Kishida T, Mazda O, Toyoda M, Tomitaka A, Ota S, Ishii R, Takemura Y, Watanabe M, Umezawa A, Gojo S. *Nanomedicine.* 2014; 10:1165–74. [PubMed: 24709330]
14. Huang RY, Chiang PH, Hsiao WC, Chuang CC, Chang CW. *Langmuir.* 2015; 31:6523–6531. [PubMed: 25989343]
15. Tomitaka A, Ueda K, Yamada T, Takemura Y. *J. Magn. Magn. Mater.* 2012; 324:3437–3442.
16. Tomitaka A, Yamada T, Takemura Y. *J. Nanomater.* 2012; 2012:1–5.
17. Tassa C, Shaw SY, Weissleder R. *Acc. Chem. Res.* 2011; 44:842–852. [PubMed: 21661727]
18. Tong S, Hou S, Zheng Z, Zhou J, Bao G. *Nano Lett.* 2010; 10:4607–4613. [PubMed: 20939602]
19. Yang H, Zhuang Y, Sun Y, Dai A, Shi Xiangyang X, Wu D, Li F, Hu H, Yang S. *Biomaterials.* 2011; 32:4584–4593. [PubMed: 21458063]
20. Cheng KK, Chan PS, Fan S, Kwan SM, Yeung KL, Wáng YXJ, Chow AHL, Wu EX, Baum L. *Biomaterials.* 2015; 44:155–172. [PubMed: 25617135]

21. Ding H, Sagar V, Agudelo M, Pilakka-Kanthikeel S, Atluri VSR, Raymond A, Samikkannu T, Nair MP. *Nanotechnology*. 2014; 25:055101. [PubMed: 24406534]
22. Kaushik A, Jayant RD, Nikkhah-Moshaie R, Bhardwaj V, Roy U, Huang Z, Ruiz A, Yndart A, Atluri V, El-Hage N, Khalili K, Nair M. *Sci. Rep.* 2016; 6:25309. [PubMed: 27143580]
23. Eustis S, el-Sayed M. a. *Chem. Soc. Rev.* 2006; 35:209–217. [PubMed: 16505915]
24. Zeng S, Yong K-T, Roy I, Dinh X-Q, Yu X, Luan F. *Plasmonics*. 2011; 6:491–506.
25. Li Y, Schluesener HJ, Xu S. *Gold Bull.* 2010; 43:29–41.
26. Wang LV, Hu S. *Science (80-.)*. 2012; 335:1458–1462.
27. Xu C, Tung GA, Sun S. *Chem Mater.* 2008; 20:4167–4169. [PubMed: 19079760]
28. Kennedy LC, Bickford LR, Lewinski NA, Coughlin AJ, Hu Y, Day ES, West JL, Drezek RA. *Small*. 2011; 7:169–183. [PubMed: 21213377]
29. Lin J, Zhou W, Kumbhar A, Wiemann J, Fang J, Carpenter EE, O'Connor CJ. *J. Solid State Chem.* 2001; 159:26–31.
30. Lyon JL, Fleming DA, Stone MB, Schiffer P, Williams ME. *Nano Lett.* 2004; 4:719–723.
31. Xing Y, Jin Y-Y, Si J-C, Peng M-L, Wang X-F, Chen C, Cui Y-L. *J. Magn. Magn. Mater.* 2014; 380:150–156.
32. Brown KR, Walter DG, Natan MJ. *Chem. Mater.* 2000; 12:306–313.
33. Brown KR, Natan MJ. *Langmuir*. 1998; 14:726–728.
34. Hien Pham TT, Cao C, Sim SJ. *J. Magn. Magn. Mater.* 2008; 320:2049–2055.
35. Sayed FN, Polshettiwar V. *Sci. Rep.* 2015; 5:9733. [PubMed: 25939969]
36. Frens G. *Nat. Phys. Sci.* 1973; 241:20–22.
37. Ji X, Song X, Li J, Bai Y, Yang W, Peng X. *J. Am. Chem. Soc.* 2007; 129:13939–13948. [PubMed: 17948996]
38. Goia DV, Matijevi E. *Colloids Surfaces A Physicochem. Eng. Asp.* 1999; 146:139–152.
39. Nam J, Won N, Jin H, Chung H, Kim S. *J. Am. Chem. Soc.* 2009; 131:13639–13645. [PubMed: 19772360]
40. Gupta AK, Gupta M. *Biomaterials*. 2005; 26:3995–4021. [PubMed: 15626447]
41. Wilczewska AZ, Niemirowicz K, Markiewicz KH, Car H. *Pharmacol. Reports*. 2012; 64:1020–1037.
42. Mandal M, Kundu S, Ghosh SK, Panigrahi S, Sau TK, Yusuf SM, Pal T. *J. Colloid Interface Sci.* 2005; 286:187–194. [PubMed: 15848416]
43. Xu Z, Hou Y, Sun S. *J. Am. Chem. Soc.* 2007; 129:8698–8699. [PubMed: 17590000]
44. Berkowitz AE, Schuele WJ, Flanders PJ. *J. Appl. Phys.* 1968; 39:1261–1263.
45. Yavuz CT, Mayo JT, Yu WW, Prakash A, Falkner JC, Yean S, Cong L, Shipley HJ, Kan A, Tomson M, Natelson D, Colvin VL. *Science*. 2006; 314:964–947. [PubMed: 17095696]
46. Jing L, Liang X, Deng Z, Feng S, Li X, Huang M, Li C, Dai Z. *Biomaterials*. 2014; 35:5814–5821. [PubMed: 24746962]
47. Xing H, Bu W, Zhang S, Zheng X, Li M, Chen F, He Q, Zhou L, Peng W, Hua Y, Shi J. *Biomaterials*. 2012; 33:1079–1089. [PubMed: 22061493]
48. Lee N, Choi SH, Hyeon T. *Adv. Mater.* 2013; 25:2641–2660. [PubMed: 23553799]
49. Li Y, Liu J, Zhong Y, Zhang J, Wang Z, Wang L, An Y, Lin M, Gao Z, Zhang D. *Int. J. Nanomedicine*. 2011; 6:2805–19. [PubMed: 22131827]
50. Salado J, Insausti M, Lezama L, Gil de Muro I, Moros M, Pelaz B, Grazu V, de la Fuente JM, Rojo T. *Nanotechnology*. 2012; 23:315102. [PubMed: 22802157]
51. Mohammad F, Balaji G, Weber A, Uppu RM, Kumar CSSR. *J. Phys. Chem. C. Nanomater. Interfaces*. 2010; 114:19194–19201. [PubMed: 21103390]
52. Ren J, Shen S, Pang Z, Lu X, Deng C, Jiang X. *Chem. Commun.* 2011; 47:11692.
53. Narayanan S, Sathy BN, Mony U, Koyakutty M, Nair SV, Menon D. *ACS Appl. Mater. Interfaces*. 2012; 4:251–260. [PubMed: 22103574]
54. Zlokovic BV. *Neuron*. 2008; 57:178–201. [PubMed: 18215617]
55. Wilhelm I, Fazakas C, Krizbai IA. *Acta Neurobiol Exp.* 2011; 71:113–128.

56. Raymond AD, Diaz P, Chevelon S, Agudelo M, Yndart-Arias A, Ding H, Kaushik A, Jayant RD, Nikkhah-Moshaie R, Roy U, Pilakka-Kanthikeel S, Nair MP. *J. Neurovirol.* 2016; 22:129–139. [PubMed: 26631079]

Author Manuscript

Author Manuscript

Author Manuscript

Author Manuscript

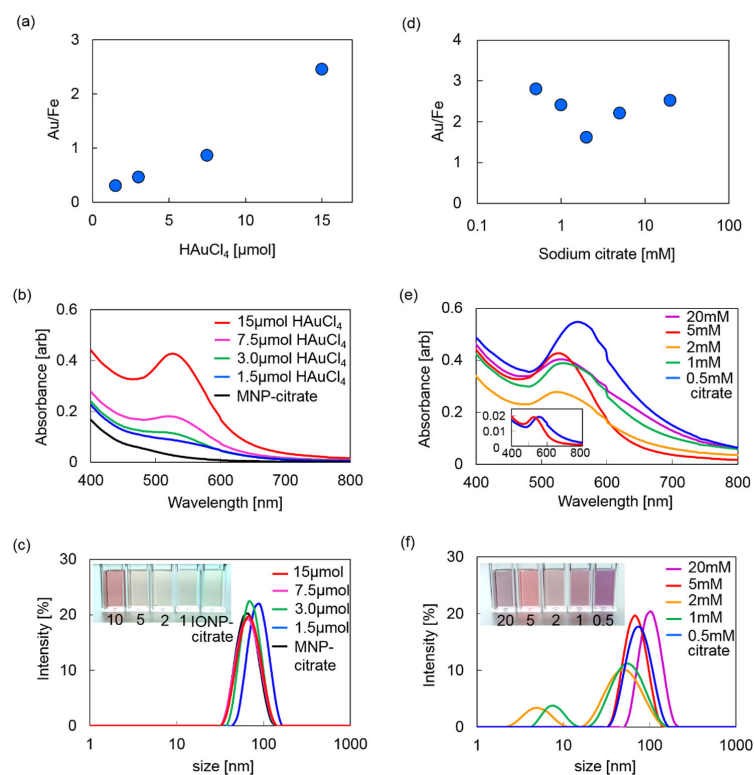


Fig. 1. Au to Fe weight ratio (a), absorbance (b), and hydrodynamic sizes (c) of MNP-citrate and MNP@Au synthesized with initial HAuCl_4 varied from 1.5 to 15 μmol and fixed concentration of sodium citrate (5 mM). Au to Fe weight ratio (d), absorbance (e), and hydrodynamic sizes (f) of MNP@Au synthesized with initial HAuCl_4 of 15 μmol and sodium citrate concentrations varied from 0.5 to 20 mM. All the samples for UV-vis and hydrodynamic size measurements were prepared at Fe concentration of 10 $\mu\text{g}/\text{ml}$. Inset: Absorbance of MNP@Au synthesized with 0.5 and 5 mM sodium citrate per unit mass of Au, and pictures MNP@Au samples.

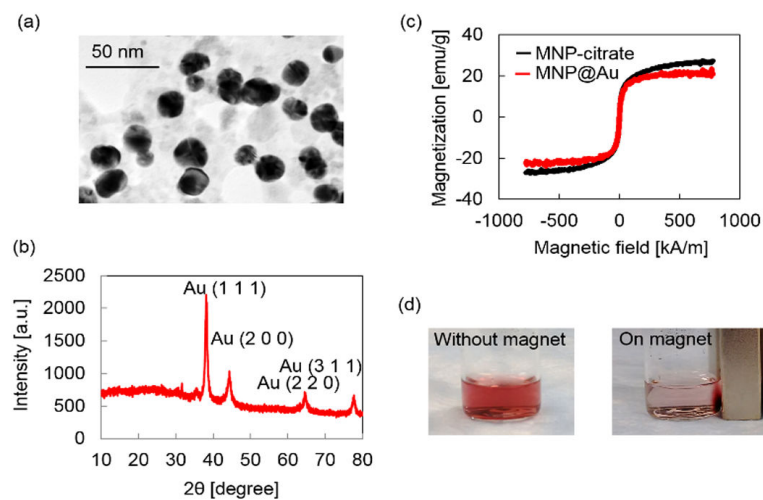


Fig. 2. TEM image of MNP@Au (a), X-ray diffraction (XRD) patterns of MNP@Au (b), magnetization curves of MNP-citrate and MNP@Au (c), and picture of MNP@Au attracted by magnet (d). The average diameter of MNP@Au was 14.5 nm. MNP@Au showed superparamagnetic property and Au specific diffraction pattern.

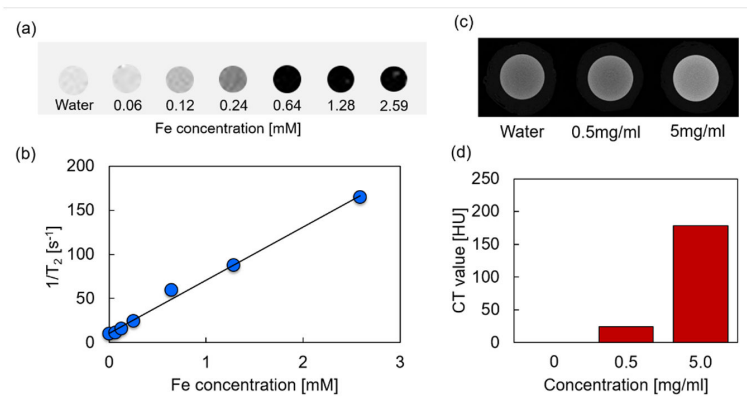


Fig. 3. T_2 -weighted MRI images (a), transverse relaxivity (b), micro-CT images (c), and CT values (d) of MNP@Au. MRI images showed strong negative contrast in a Fe concentration dependent manner, and linear correlation between transverse relaxivity and Fe concentration was observed. Micro-CT images showed concentration dependent positive contrast and increase of CT values with nanoparticle concentration.

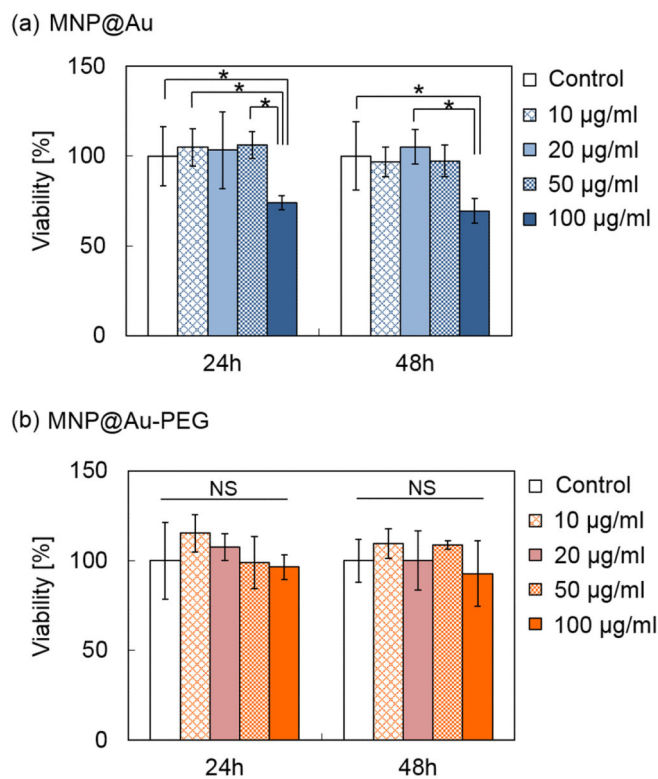
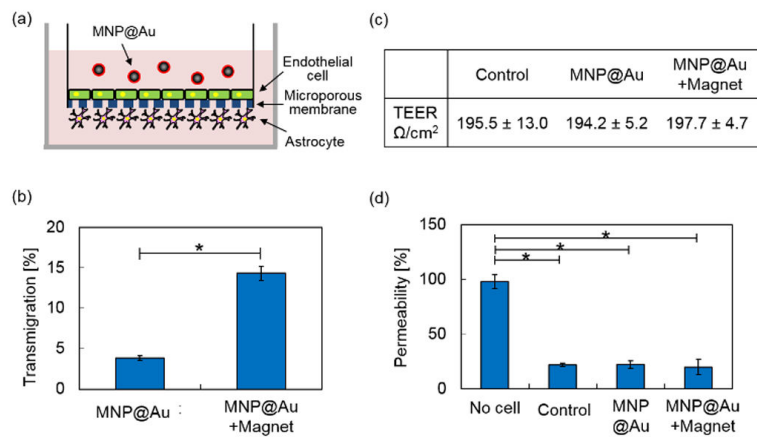


Fig. 4. Viability of human primary astrocytes after 24h and 48h exposure to MNP@Au (a) and MNP@Au-PEG (b) determined using XTT assay. (* $P < 0.05$; NS, not significant, $P > 0.05$; $N = 3$) Viability reduction was observed after exposing MNP@Au at the concentration of 100 µg/ml. In contrast, no reduction was observed for the astrocytes exposed to PEG coated MNP@Au.

**Fig. 5.**

(a) Schematic illustration of *in vitro* blood brain barrier (BBB) model, (b) transmigration of PEG coated MNP@Au across an *in vitro* BBB model, (c) transendothelial electrical resistance (TEER) values of the *in vitro* BBB model after exposure to PEG coated MNP@Au, and (d) effect of PEG coated MNP@Au exposure on fluorescein isothiocyanate-dextran transfer in the BBB model. (*P < 0.05; N = 3)

Table 1

Synthesis conditions and characterizations of MNP@Au synthesized with initial H₂AuCl₄ of 15 μ mol and sodium citrate concentration varied from 0.5 to 20 mM.

Sodium citrate	H ₂ AuCl ₄	pH	Hydrodynamic size	SPR peak
20 mM	15 μ mol	7.0	95 \pm 31 nm	531 nm
5 mM	15 μ mol	7.0	57 \pm 26 nm	526 nm
2 mM	15 μ mol	6.0	Polydispersed	523 nm
1 mM	15 μ mol	5.5	polydispersed	533 nm
0.5 mM	15 μ mol	3.2	64 \pm 27 nm	556 nm